

MirrorGaussian: Reflecting 3D Gaussians for Reconstructing Mirror Reflections

Jiayue Liu^{1*}, Xiao Tang^{2*}, Freeman Cheng³, Roy Yang², Zhihao Li^{2†},
Jianzhuang Liu⁴, Yi Huang⁴, Jiaqi Lin¹, Shiyong Liu², Xiaofei Wu²
Songcen Xu², and Chun Yuan^{1†}

¹Tsinghua University ²Huawei Noah’s Ark Lab

³University of Toronto ⁴University of Chinese Academy of Sciences

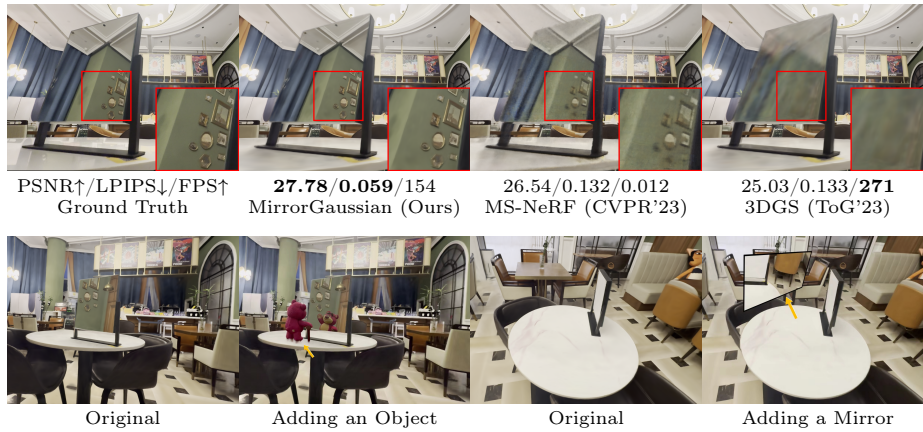


Fig. 1: The ground truth and renderings of our MirrorGaussian and state-of-the-art methods in the *Coffee-House* scene from our dataset. Compared to existing methods, our MirrorGaussian achieves both high-quality and real-time rendering (top row), and empowers scene editing such as inserting new objects and mirrors (bottom row).

Abstract. 3D Gaussian Splatting showcases notable advancements in photo-realistic and real-time novel view synthesis. However, it faces challenges in modeling mirror reflections, which exhibit substantial appearance variations from different viewpoints. To tackle this problem, we present MirrorGaussian, the first method for mirror scene reconstruction with real-time rendering based on 3D Gaussian Splatting. The key insight is grounded on the mirror symmetry between the real-world space and the virtual mirror space. We introduce an intuitive dual-rendering strategy that enables differentiable rasterization of both the real-world 3D Gaussians and the mirrored counterpart obtained by reflecting the former about the mirror plane. All 3D Gaussians are jointly optimized with the mirror plane in an end-to-end framework. MirrorGaussian achieves high-quality and real-time rendering in scenes with mirrors, empowering

The work was done during an internship at Huawei.

* Equal contribution † Corresponding authors

scene editing like adding new mirrors and objects. Comprehensive experiments on multiple datasets demonstrate that our approach significantly outperforms existing methods, achieving state-of-the-art results. Project page: <https://mirror-gaussian.github.io/>.

Keywords: Novel View Synthesis · Mirror Reflections · 3D Gaussian Splatting · Real-Time Rendering

1 Introduction

Reconstructing 3D scenes from multi-view images for photo-realistic rendering is a fundamental problem in computer vision and graphics, with wide-ranging applications in cinematography, simulation, virtual and augmented reality, *etc.* A notable breakthrough in this area is Neural Radiance Field (NeRF) [25] introduced in 2020. NeRF intensively samples points via ray marching, utilizes multi-layer perceptrons (MLPs) to estimate density and view-dependent colors for each point, and then adopts volume rendering to generate photo-realistic rendering results. More recently, 3D Gaussian Splatting (3DGS) [16] emerges and gains a lot of attention [4, 14, 15, 22, 24, 43, 45]. 3DGS employs point clouds to represent scenes, where each point has opacity and anisotropic 3D Gaussian properties to model its shape, and uses a set of coefficients of spherical harmonic (SH) functions to model its view-dependent colors. Through efficient point-based differentiable rasterization, 3DGS achieves high-quality and real-time rendering simultaneously.

However, both NeRF and 3DGS have limitations in accurately reconstructing scenes containing mirrors, due to their inherent reliance on multi-view consistency. Mirrors have highly specular reflections, which causes inconsistencies between the front and back views of the mirror. As a result, the appearance of the same point can vary significantly when observed from different viewpoints. It is challenging to model such appearance variation through MLPs or SH functions [15, 23, 41, 44]. This challenge leads to a situation where mirror rendering is often blurry (see Figure 1) or floaters appear behind the mirror.

Some researchers propose NeRF-based approaches to reconstruct scenes with mirror reflections [44, 46]. MS-NeRF [44] introduces a multi-space scheme that constructs the scene with multiple sub-spaces, and utilizes a gate MLP that controls the visibility of a certain sub-space to obtain the final rendering results. Mirror-NeRF [46] and TraM-NeRF [35] trace reflected rays physically in the scene to optimize a unified NeRF model. While these NeRF-based approaches demonstrate some success in reconstructing mirror reflections, they still face limitations. Specifically, they require expensive point sampling and MLP queries for rendering, leading to slow optimization and rendering. Since these methods are designed for ray marching, they cannot be directly adopted by rasterization to achieve fast rendering.

In this paper, we introduce MirrorGaussian, which integrates an explicit point-cloud-based representation extended from 3DGS for 3D reconstruction with mirror reflections. MirrorGaussian achieves photo-realistic and real-time

novel view synthesis with a rasterization-based dual-rendering strategy. The fundamental insight is grounded in the principle of mirror reflection, which indicates the mirror symmetry between the real-world scene outside the mirror and the reflected scene inside the virtual mirror space. Drawing from this principle, we intuitively propose a dual-rendering strategy, which utilizes both the real-world image and its corresponding mirror image to synthesize novel views. The real-world image is synthesized from the real-world 3DGS point cloud. The mirror image, on the other hand, is derived by reflecting the real-world 3DGS point cloud across the mirror plane. To acquire the mirror plane equation, we first obtain a rough estimate from the sparse point cloud generated using Structure-from-Motion (SfM) [30], and then jointly optimize it with 3D Gaussians to achieve higher accuracy. With the real-world 3D Gaussians and its mirrored counterpart, we apply the point-based rasterization [16] to get both the real-world and the mirror images. We then compose them using the corresponding mirror mask to get the final rendering result. To obtain the mirror mask from arbitrary viewpoints, we need to locate the mirror points in 3D space. Thus, we augment 3D Gaussians with an extra mirror label, which indicates whether a point belongs to the mirror surface or not. We can then render these 3D Gaussians to generate a mirror mask from any viewpoint.

We conduct comprehensive experiments on several datasets and demonstrate that MirrorGaussian significantly outperforms existing methods both quantitatively and qualitatively. We facilitate free-viewpoint navigation with real-time performance, thanks to the efficient point-based rasterization and the freedom from any neural network. Since MirrorGaussian utilizes explicit point clouds to represent scenes, it additionally enables various applications in scene editing, such as integration of new objects into the scene, and placing a new mirror, *etc.* In summary, the main contributions of this paper are threefold:

- We present MirrorGaussian, the first method that achieves high-fidelity reconstruction and real-time rendering of scenes containing mirrors, empowering various applications in scene editing.
- We propose a novel representation of scenes with mirrors for point-based rendering, which contains both the real-world 3DGS point cloud and its mirrored counterpart, obtained by reflecting the former across the mirror plane.
- We introduce intuitive dual-rendering strategy that enables differentiable rasterization of both the real-world and the mirrored 3D Gaussians. This strategy facilitates the generation of plausible images in mirrors while maintaining efficiency of optimization and rendering.

2 Related Work

Novel View Synthesis (NVS). Given a set of calibrated images capturing a 3D scene, NVS aims to generate photo-realistic images from new viewpoints [5, 32, 33, 39]. A remarkable breakthrough in this field is NeRF [25].

NeRF, as an implicit representation of the scene, utilizes MLPs to estimate density and view-dependent colors for intensively sampled points via ray tracing, and then leverages volume rendering to generate novel views. While NeRF can produce photo-realistic rendering results, it suffers from high computation demands on intensive point sampling and expensive MLP queries. This leads to inefficient optimization and slow rendering, making NeRF unsuitable for interactive applications. Further advancements have been made to tackle this problem [3, 6, 7, 11, 13, 26–28]. However, it still remains challenging for NeRF-based methods to balance between quality and efficiency. Concurrently, point-based rasterization methods have shown impressive results, providing an appealing mix of rendering quality and computational efficiency [9, 10, 16, 19, 29]. A representative work is 3DGS [16], which starts gaining much attention. 3DGS explicitly represents a 3D scene with a set of anisotropic 3D Gaussians points, and each point contains opacity and a set of SH coefficients for modeling view-dependent colors. By applying a hardware-accelerated point-based rasterizer instead of computationally intensive ray tracing, 3DGS achieves both high-quality rendering and real-time rendering at the same time. Lately, there have been a lot of work on further enhancing the quality of 3DGS [20, 22, 24, 40, 45]. Scaffold-GS [24] proposes an anchor-based approach to distribute 3D Gaussians, which delivers higher rendering quality. Mip-Splatting [45] identifies the aliasing problem in 3DGS and introduces a 3D smoothing filter and a 2D Mip filter to produce alias-free results. However, both NeRF-based and 3DGS-based methods still struggle with reconstructing scenes with mirrors. Mirrors have highly specular reflections, which can vary significantly from different viewpoints. It remains challenging for existing methods to model such variation using MLPs or SH functions.

Reflection Reconstruction. Some studies have started to tackle the reflection reconstruction via NeRF [12, 23, 34, 42] or point-based rendering [15, 18, 21, 31]. One common approach is decomposing diffuse colors and specular colors from the objects by physically-based rendering (PBR). NeRO [23] first reconstructs the geometry of the object using NeuS [38], and then recovers the environment lights and the materials of the object via PBR to calculate specular colors. GaussianShader [15] extends 3DGS to extract the normal of the reflective object from the shortest axis directions of 3D Gaussians, and similarly optimizes an environment lighting map for rendering reflective appearances. These methods mostly rely on optimizing the environment lighting map; while it might be sufficient for object-level reconstruction, it is often too rough to model reflections in the mirror. Another direction is to model the real-world and the reflected elements separately, and then combine them with appropriate weights to render the final image. Ref-NeRF [36] reparameterizes NeRF’s color MLP to predict reflection colors from reflected view directions about estimated normal vectors. NeRF-ReN [12] models both a real-world radiance field and a reflected radiance field. The images rendered from these two fields are further blended using an optimizable weight. UniSDF [37] estimates the SDF of the scene to predict surface normals, and similarly optimizes two radiance fields and blending weights. The

reflective radiance field takes the reflected view direction derived from the surface normal as input to better capture reflective colors. As for point-based rendering, Kopanas *et al.* [18] reconstruct both real-world and reflected point clouds, and use an MLP to model curved reflectors’ trace of reflection inside the object to reconstruct reflections. While these methods achieve separate optimization for real-world and reflective elements, they fail to consider the correspondence between the two. This oversight may limit the ability to reconstruct high-fidelity details from mirror reflections, thus compromising overall rendering quality.

Mirror Reflection Reconstruction. There are some NeRF-based methods that specifically address the challenge of reconstructing mirror reflections. MS-NeRF [44] innovates by decomposing the scene into multiple subspaces, each represented by a neural feature field. To render the scene, they sample points in these subspaces to get multiple feature maps. These feature maps are passed through a decoder MLP to get multiple rendered images. A gate MLP is then applied to compose these images into the final rendering result. Mirror-NeRF [46] optimizes a unified NeRF by tracing rays on reflective surfaces using the estimated normals. Additionally, it estimates the reflection probabilities of surface to blend the colors of camera rays and reflected rays, then synthesizes the final image. TraM-NeRF [35], a concurrent work, employs a similar ray-tracing strategy and introduces a radiance estimator that combines volume and reflected radiance integration to reduce the number of sampled points along rays.

However, these methods still rely on inefficient ray marching and expensive MLP queries. This results in heavy computation loads, making them impractical for interactive usage. In contrast, our MirrorGaussian excels in superior reconstruction quality and fast rendering, positioning it as a promising solution for various applications in scene editing.

3 Preliminaries

3DGS represents the scene with Q anisotropic 3D Gaussian primitives $\{\mathcal{G}_i | i = 1, \dots, Q\}$:

$$\mathcal{G}_i(x) = e^{-\frac{1}{2}(x-\mu_i)^T \Sigma_i^{-1}(x-\mu_i)}, \quad (1)$$

where $\mu_i \in \mathbb{R}^3$ denotes \mathcal{G}_i ’s center (mean) and $\Sigma_i \in \mathbb{R}^{3 \times 3}$ denotes its 3D covariance matrix defined in the world space. To maintain its positive semi-definiteness, Σ_i is decomposed as an ellipsoid using a scaling matrix $S_i \in \mathbb{R}^{3 \times 3}$ and a rotation matrix $R_i \in \mathbb{R}^{3 \times 3}$:

$$\Sigma_i = R_i S_i S_i^T R_i^T. \quad (2)$$

Each 3D Gaussian \mathcal{G}_i is also characterized with opacity $\alpha_i \in [0, 1]$ and spherical harmonic coefficients *SHs* for view-dependent colors $c_i(d)$, where d denotes the view direction from the camera.

During the rendering process, 3D Gaussians $\mathcal{G}_i(x)$ are projected to 2D Gaussians $\mathcal{G}'_i(x)$ with $\mu'_i \in \mathbb{R}^2$ and $\Sigma'_i \in \mathbb{R}^{2 \times 2}$ via EWA Splatting [16, 47], where μ'_i

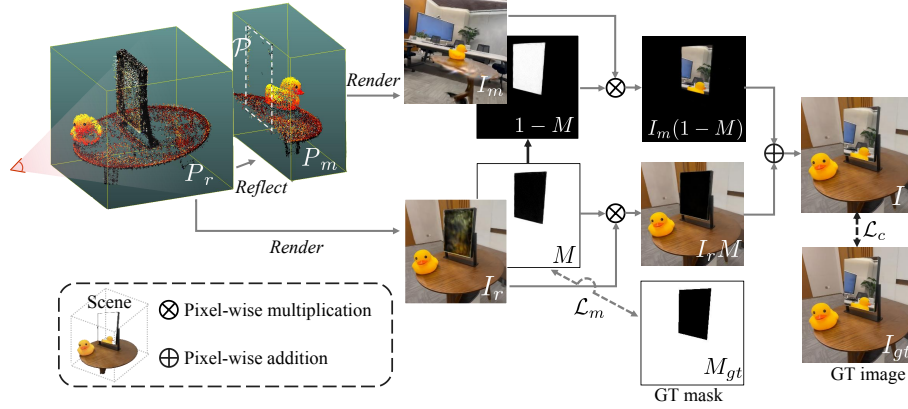


Fig. 2: Overview of MirrorGaussian. MirrorGaussian is grounded on the mirror symmetry between the real-world scene and its counterpart in the mirror. We first reflect the 3D Gaussians P_r about the mirror plane \mathcal{P} to obtain its mirrored counterpart P_m . Then, we rasterize P_r to get the real-world image I_r and the mirror mask M , and rasterize P_m to get the mirror image I_m . The final image I is composed by I_r and I_m using M . I and M are supervised by the captured image I_{gt} and its annotated mirror mask M_{gt} , respectively. Note that for the sake of visual simplicity, P_r and P_m have been cropped.

and Σ'_i denotes the center (mean) and the 2D covariance matrix of \mathcal{G}'_i in the image space, respectively. $\{\mathcal{G}'_i\}$ are then assigned to different tiles, sorted and alpha-blended into a rendered image in a point-based volume rendering manner. The color C of a pixel p is computed via alpha blending:

$$C = \sum_{i \in N} c_i(d) \alpha_i \mathcal{G}'_i(p) T_i, \quad T_i = \prod_{j=1}^{i-1} (1 - \alpha_j \mathcal{G}'_j(p)), \quad (3)$$

$$\mathcal{G}'_i(p) = e^{-\frac{1}{2}(p - \mu'_i)^T \Sigma'^{-1}_i (p - \mu'_i)},$$

where N denotes the set of ordered 2D Gaussians overlapping the pixel. Leveraging the differentiable tile-based rasterizer, all attributes of 3D Gaussians are optimized end-to-end efficiently via the combination of the \mathcal{L}_1 and D-SSIM losses:

$$\mathcal{L}_c = (1 - \lambda) \mathcal{L}_1 + \lambda \mathcal{L}_{D-SSIM}, \quad (4)$$

where λ is a balance parameter. This process is interleaved with adaptive point densification and pruning to better represent the scene [16].

4 Method

The overview of MirrorGaussian is illustrated in Fig. 2. MirrorGaussian reconstructs a static scene containing a mirror from multiple-view images, along with

their corresponding camera poses and mirror masks, and a sparse point cloud obtained from Structure from Motion (SfM) [30]. The core idea of MirrorGaussian is derived from the principle of mirror reflection: a scene in the real world and its reflected counterpart in the virtual mirror space are mirror-symmetrical about the mirror plane. Leveraging this principle, we propose a dual-rendering strategy, which renders both the real-world image I_r outside the mirror and the corresponding mirror image I_m , and fuses them to get the final rendering result. Based on our dual-rendering strategy, we further propose a three-stage pipeline for end-to-end optimization of reconstructing scenes containing mirrors. First, we start by optimizing 3DGS in an unmodified manner to get the real-world 3D Gaussians P_r . Next, we reflect P_r to get the mirrored 3D Gaussians P_m in the mirror space, and optimize the mirror plane equation via our dual-rendering strategy while fixing other parameters. Finally, we augment P_r with a mirror label for generating the mirror mask in any viewpoints. We jointly optimize 3D Gaussians with the mirror label and the mirror plane equation to achieve high-fidelity reconstruction with mirror reflection.

In the following subsections, we first explain how to reflect P_r to get mirrored 3D Gaussians P_m given the mirror plane equation (Sec. 4.1). Next, we present a method that obtains a rough mirror plane equation from the sparse SfM point cloud, and jointly optimize it with 3D Gaussians via our dual-rendering strategy (Sec. 4.2). Finally, we describe how to optimize the 3D mirror mask, enabling high-quality rendering of mirror reflections from arbitrary viewpoints (Sec. 4.3).

4.1 3D Gaussians Reflection about the Mirror Plane

This subsection explains how to reflect the 3D Gaussians P_r across the mirror plane \mathcal{P} (the acquisition of \mathcal{P} is detailed in Sec. 4.2) to get the mirrored 3D Gaussians P_m for modeling the virtual mirror space. We parameterize the mirror plane as $\mathcal{P}(x) = \langle n, x \rangle + b = 0, x \in \mathbb{R}^3$, where $n \in \mathbb{R}^3$ denotes the normal vector of \mathcal{P} and $b \in \mathbb{R}^1$ denotes the negative of the plane’s distance from the origin along n . A mirrored 3DGS point $\hat{\mathcal{G}}$ is derived from \mathcal{G} by keeping its opacity α and scale S , but modifying its other three attributes: mean μ , rotation R and view-dependent color $c(d)$.

First, the mean $\hat{\mu}$ of $\hat{\mathcal{G}}$ can be determined using the reflection function \mathcal{F} :

$$\hat{\mu} = \mathcal{F}(\mu) = \mu - 2 \frac{\langle n, \mu \rangle + b}{\|n\|^2} n. \quad (5)$$

Next, we flip R across \mathcal{P} to get the rotation \hat{R} of $\hat{\mathcal{G}}$ (See Fig. 3(a)). By revisiting Eq. 2, we find that S is a diagonal matrix and R is an orthogonal matrix that satisfies $R^T = R^{-1}$, and thus Eq. 2 can also be interpreted as the eigendecomposition of the matrix Σ :

$$\Sigma = RSS^T R^T = RS^2 R^{-1}, R^{-1} \Sigma R = S^2. \quad (6)$$

Therefore, the columns of R , denoted as R_1, R_2 and R_3 , are the normalized eigenvectors of Σ . Given that Σ also describes the configuration of a Gaussian

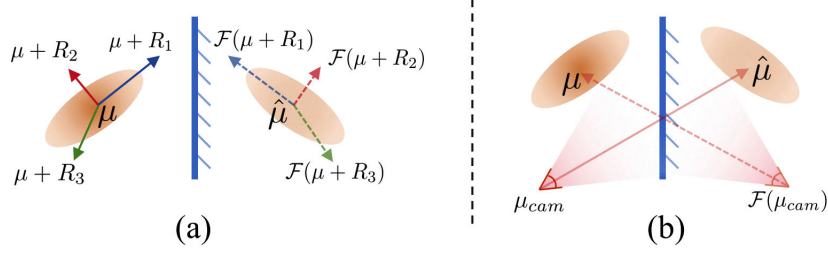


Fig. 3: Reflecting a real-world 3D Gaussian \mathcal{G} with mean μ and rotation R about the mirror plane (blue line) to get the mirrored 3D Gaussian $\hat{\mathcal{G}}$. (a) illustrates how the mean $\hat{\mu}$ and the rotation \hat{R} of the mirrored 3D Gaussian $\hat{\mathcal{G}}$ are derived using the reflection function \mathcal{F} . (b) illustrates how we derive the view-dependent color of $\hat{\mathcal{G}}$. Instead of modifying the SH coefficients according to the reflection, we directly reflect the view direction for $\hat{\mathcal{G}}$ to get the view-dependent color.

ellipsoid [16], R_1 , R_2 and R_3 represent the directions of the three principal axes of the Gaussian ellipsoid in the 3D space. Based on it, $\hat{R} = (\hat{R}_1, \hat{R}_2, \hat{R}_3)$ is obtained by reflecting R_1 , R_2 , R_3 over \mathcal{P} :

$$\hat{R}_i = \mathcal{F}(\mu + R_i) - \hat{\mu}, \quad i = 1, 2, 3. \quad (7)$$

Last but not least, the view-dependent colors $c(d)$ should also be flipped to get $\hat{c}(d)$ in the mirror space. 3DGS uses a set of SH coefficients to model view-dependent colors $c(d)$, but it is complex to directly compute these coefficients after reflecting. Thus, instead of computing them, we mirror d when rendering $\hat{\mathcal{G}}$, as illustrated in Fig. 3(b). Then $\hat{c}(d)$ can be derived by:

$$\hat{c}(d) = c(\hat{d}), \quad \hat{d} = \mu - \mathcal{F}(\mu_{cam}), \quad (8)$$

where μ_{cam} is the coordinate of the camera.

4.2 Mirror Plane Equation Estimation

We need to acquire the accurate mirror plane equation via optimization to enable the mirroring process. To reduce the difficulty of optimization, we start from a rough estimation of \mathcal{P} , which is derived from the input sparse point cloud generated from SfM. Fig. 4 illustrates the procedure of obtaining this rough estimation. Given the mirror mask of an image (derived from SAM [17]), we extract the mask edges and dilate it to get the 2D mirror border. Next, we identify 3D points from the sparse SfM point cloud that fall on the extracted 2D border. This is achieved by leveraging the correspondences between 2D points in the images and 3D points in the point cloud, which is established by SfM. We apply this operation to all input images to aggregate 3D points that locate on the mirror border from the SfM point cloud, then remove flying points, and finally use RANSAC [8] to fit a plane to the 3D points as the rough estimation of the mirror plane.

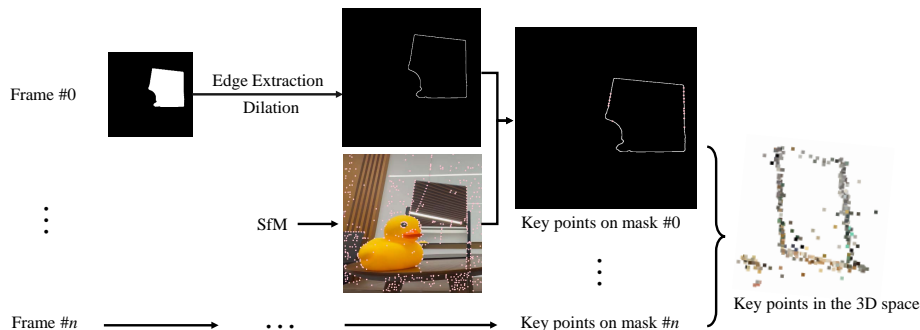


Fig. 4: Strategy for yielding the mirror’s initial position. The mirror’s edges from each frame’s mask are extracted using dilation and erosion. Employing SfM, corresponding 2D-3D point pairs are established, allowing reconstruction of 3D points along the mirror edges. Finally, a plane is fitted to the aggregated 3D points from all frames.

Since this mirror plane estimation may not be accurate enough, we further jointly optimize it with 3D Gaussians, which is incorporated into our three-stage optimization pipeline. In detail, in the first optimization stage, we train vanilla 3DGS for s_1 steps to get the real-world 3D Gaussians P_r . Next, we mirror P_r about the roughly estimated \mathcal{P} to get P_m . Note that we only mirror 3D Gaussian points that are in front of the mirror plane. Points behind the mirror plane are not reflected and thus have no contribution to the mirror image. For the next s_2 steps in our second optimization stage, we render both P_r and P_m to get the real-world image I_r and the mirror image I_m , and then fuse them together using the ground-truth mask M_{gt} obtained by SAM [17] to get the final rendering image I :

$$I = I_r \odot M_{gt} + I_m \odot (1 - M_{gt}). \quad (9)$$

We supervise I using the captured image I_{gt} with the \mathcal{L}_1 loss and D-SSIM loss. To enhance optimization stability and ensure accurate estimation of the mirror plane equation, we only backpropagate the gradients to the parameters of the mirror plane \mathcal{P} . Optimizable parameters of P_r are fixed during the second optimization stage. After s_2 steps, the mirror plane equation is further optimized in our final optimization stage, which will be detailed in Sec. 4.3.

4.3 3D Mirror Mask

With our dual-rendering strategy based on the accurate mirror plane equation, we can already generate plausible renderings if the mirror masks are provided. However, to synthesize novel views, we need to acquire the mirror mask M from arbitrary viewpoints. Thus, in the third optimization stage with s_3 steps, our main goal is to identify 3DGS points \mathcal{G} that are located on the mirror surface. By rendering these mirror points, we can generate mirror masks from novel views.

Mirror Label. We assign a label $k \in [0, 1]$ for each \mathcal{G} with value zero when it belongs to the mirror surface and one when it does not. We can then render the mirror mask M by applying the same alpha blending from 3DGS as described in Eq. 3:

$$K = \sum_{i \in N} k_i \alpha_i \mathcal{G}'_i(p) T_i, \quad T_i = \prod_{j=1}^{i-1} (1 - \alpha_j \mathcal{G}'_j(p)), \quad (10)$$

where $K \in [0, 1]$ is the value of the pixel p in M , denoting how likely p belongs to the mirror.

In the third optimization stage, we add mirror labels k to all 3D Gaussians and initialize them based on the distance of 3D Gaussians' means μ to the mirror plane. We set $k = 1$ when the distance exceeds a threshold $\tau = 0.1$, indicating that the point does not belong to the mirror. For the remaining 3D Gaussians, k is randomly assigned between 0 and 1.

RGB Rendering Formula with the Mirror Label. We require points with $k \approx 0$ to be distributed over the mirror surface to enable accurate mirror mask rendering. Meanwhile we do not want these points to contribute to the rendering of I , as they may hinder the rendering of P_m . To achieve so in a differentiable way, we modify the vanilla color rendering formula in Eq. 3 by multiplying α with k . The color C of a pixel p is then computed as:

$$C = \sum_{i \in N} c_i(d) \alpha'_i \mathcal{G}'_i(p) T'_i, \quad T'_i = \prod_{j=1}^{i-1} (1 - \alpha'_j \mathcal{G}'_j(p)), \quad \alpha'_j = \alpha_j k_j. \quad (11)$$

In the third optimization stage, we fuse the real-world image I_r and the mirror image I_m using the estimated mirror mask M instead of M_{gt} to get the final image I :

$$I = I_r \odot M + I_m \odot (1 - M). \quad (12)$$

We also supervise I by computing the \mathcal{L}_1 loss and D-SSIM loss between I and the captured image I_{gt} . To supervise M , we add the mask loss \mathcal{L}_m , which is the \mathcal{L}_1 loss between M and M_{gt} . We further add a regularization term \mathcal{L}_d that encourages the 3D Gaussians belonging to the mirror surface to be close to the mirror plane:

$$\mathcal{L}_d = \frac{1}{Q} \sum_{i=1}^Q \left[\frac{|\langle n, \mu \rangle + b|}{\|n\|} (1 - k_i) \right]^2, \quad (13)$$

where Q is the total number of the 3D Gaussians. This loss effectively helps the mirror points to fast converge towards the mirror plane.

In the third optimization stage, we optimize all 3D Gaussian attributes, including the newly introduced mirror label k and the mirror plane \mathcal{P} , but tune

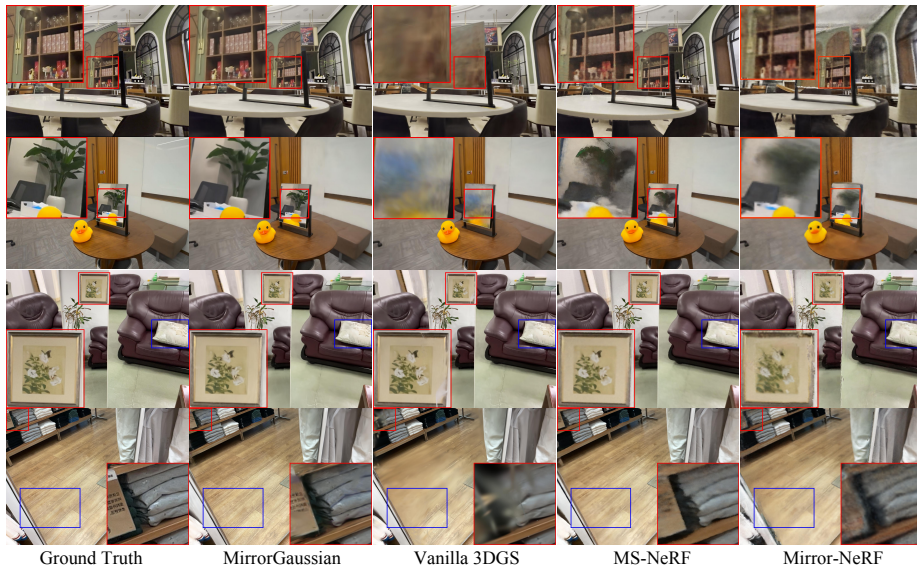


Fig. 5: Reconstructed samples with different methods across various scenes. Top row: *Meeting Room*. Second row: *Coffee House*. Third row: *Lounge*. Bottom row: *Market*.

down the learning rate of \mathcal{P} for stability. We incorporate all the loss functions mentioned above to obtain the training loss for our final optimization stage:

$$\mathcal{L} = \mathcal{L}_c + \lambda_m \mathcal{L}_m + \lambda_d \mathcal{L}_d, \quad (14)$$

where $\lambda_m = 0.2$ and $\lambda_d = 0.1$ are two balance hyperparameters. Note that the optimization losses for the first and second stages are both \mathcal{L}_c only.

Implementation Details. The training steps of the three stages s_1 , s_2 , and s_3 are 20,000, 1,000 and 9,000, respectively. We use the Adam optimizer and exponentially decay the learning rate of \mathcal{P} from $1.6e-4$ to $1.6e-6$ in the second stage. In the third stage, the learning rate of \mathcal{P} is decayed from $1.6e-6$ to $1.6e-8$ exponentially, and the learning rate of k is set to 0.005.

5 Experiments

5.1 Experiment Setup

Compared Methods. We compare MirrorGaussian with the most relevant state-of-the-art methods: vanilla 3DGS [16], MS-NeRF [44], Mirror-NeRF [46], and Ref-NeRF [36]. For vanilla 3DGS, we optimize it on four scenes under the same setting described in its original paper [16]. For MS-NeRF, we choose Mip-NeRF 360 [2] based model with eight sub-spaces that shows the best quality. For Mirror-NeRF, we use the iNGP [26] based model for training efficiency.

Table 1: Quantitative evaluation of our method compared to previous works on four real-world scenes containing mirrors. We report SSIM \uparrow , PSNR \uparrow and LPIPS \downarrow , as well as training time and FPS on test views. The **best** and second best results are highlighted.

Scene	<i>Coffee-House</i>			<i>Meeting-Room</i>			<i>Market</i>			<i>Lounge</i>			<i>Average (Avg.)</i>	
Metrics	SSIM	PSNR	LPIPS	SSIM	PSNR	LPIPS	SSIM	PSNR	LPIPS	SSIM	PSNR	LPIPS	Avg. FPS	Avg. Time
MS-NeRF [44]	0.901	<u>26.21</u>	0.111	0.910	31.09	0.129	0.685	26.25	0.275	0.921	31.20	0.126	0.048	14h57m
Mirror-NeRF [46]	0.847	23.92	0.201	0.889	27.43	0.145	0.809	27.49	0.146	0.917	29.38	0.184	0.468	18h23m
Ref-NeRF [36]	0.823	23.82	0.273	0.872	29.01	0.206	0.560	23.75	0.522	0.878	28.49	0.194	0.197	9h48m
Vanilla 3DGS [16]	<u>0.921</u>	25.83	<u>0.086</u>	<u>0.939</u>	28.82	<u>0.073</u>	<u>0.832</u>	<u>28.29</u>	<u>0.127</u>	<u>0.927</u>	30.10	0.107	271	47m
MirrorGaussian	0.927	26.66	0.068	0.943	<u>30.63</u>	0.063	0.844	28.35	0.105	0.928	<u>31.10</u>	<u>0.108</u>	<u>155</u>	<u>1h8m</u>

Datasets. The experiments are conducted on four real-world scenes with mirrors: *Lounge* and *Market* from the Mirror-NeRF dataset [46], and *Meeting-Room* and *Coffee-House* captured by ourselves. *Lounge* and *Market* only include forward-facing views of the mirror and omit viewpoints capturing the back. *Meeting-Room* and *Coffee-House* capture 360-degree views of the mirror. These two scenes are captured with an iPhone 15 Pro. We use COLMAP [30] to estimate camera poses and SAM [17] to segment the mirror masks. Every 8th image is preserved for testing.

Metrics. We perform quantitative evaluation by resizing the images to 1.6 megapixels following [16] except for Mirror-NeRF. We find that Mirror-NeRF is difficult to converge at high resolution, so we keep its original setting with width of 480 pixels. We compare all the methods using three metrics: SSIM, PSNR, and AlexNet-based LPIPS. We also report the rendering speed at the image size of 1.6 megapixels, and the overall optimization time.

5.2 Result Analysis

Rendering Quality. We report the SSIM, PSNR, and LPIPS metrics in each scene in Tab. 1, and also show visual comparisons in Fig. 5. The image qualities of the NeRF-based methods are relatively low, and the reflections in the parts of mirrors are even more blurry and short of details. Vanilla 3DGS produces extremely blurry mirror surfaces when the dataset contains views behind the mirror (see the first two rows in Fig. 5). For the forward-facing scenes (the last two rows in Fig. 5), vanilla 3DGS tends to produce point clouds behind the mirrors to model the virtual mirror space. Although the rendering from frontal perspectives is relatively good, 3DGS often gets blurry results around the mirror borders due to conflicts in different viewpoints. Note that we follow Mirror-NeRF’s original setting to downscale the training images with width of 480 pixels to avoid the extremely long training time.

Training and Rendering Speeds. In Tab. 1, we also report the average training time and rendering speed. The training and rendering speed tests are

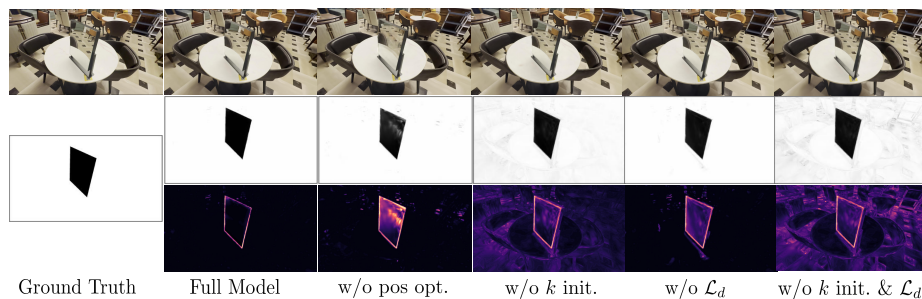


Fig. 6: Ablation studies. Bottom row: FLIP error map [1] visualization between the rendered mirror masks and the ground truth mask.

Table 2: Ablation studies on the mirror equation and mask optimization.

Model setting	SSIM \uparrow	PSNR \uparrow	LPIPS \downarrow
1) w/o mirror equation optimization	0.919	25.84	0.082
2) w/o distance-aware initialization of k	0.926	26.42	0.071
3) w/o distance loss	0.926	26.59	0.068
4) w/o both 2) and 3)	0.921	25.95	0.077
Full model	0.927	26.74	0.068

both conducted on a single NVIDIA V100 GPU. Vanilla 3DGS and MirrorGaussian require much shorter training time, and achieves real-time rendering at high resolution. MS-NeRF builds upon Mip-NeRF 360 [2] and uses eight sub-spaces to composite the final rendering, resulting in a low rendering speed. Mirror-NeRF physically models ray reflections, and samples points on incoming and outgoing lights recursively, thus requiring long training time. MirrorGaussian takes a slightly longer training time compared to vanilla 3DGS, due to the dual-rendering strategy in the final optimization stage.

5.3 Ablation Studies

We perform ablation studies on the *Coffee-House* scene to evaluate different aspects of MirrorGaussian, as illustrated in Tab. 2 and Fig. 6.

Mirror Equation Optimization. We optimize the mirror plane equation from a rough estimation in the second and final optimization stages. Without this optimization, reflecting the 3D Gaussians P_r across the mirror plane \mathcal{P} results in a shifted rendering in the mirror compared to the ground truth image I_{gt} . Consequently, the rendering results are blurry as shown in the third column of Fig. 6.

Strategies for Mask Generation. After optimizing the mirror equation, we initialize the mirror label k based on the distance of the 3D Gaussian to the

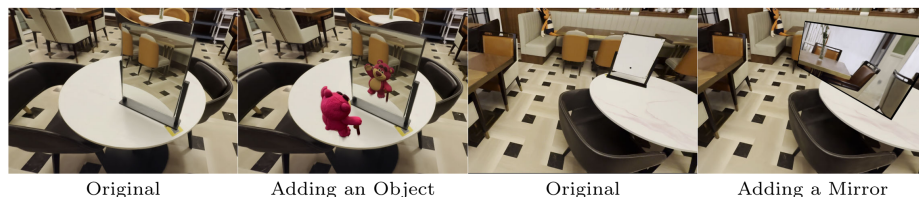


Fig. 7: Illustration of scene editing. Please check our video demos in the supplementary material.

mirror plane. This initialization accelerates the 3D mirror mask optimization and thus facilitates the optimization for colors. Besides, the distance loss \mathcal{L}_d encourages mirror points to distribute over the mirror surface. When the distance-aware k initialization is utilized, the effects of the distance loss is not notably significant, but a much worse mask M_r is produced without both.

5.4 Scene Editing

Adding New Objects. MirrorGaussian has the capability to seamlessly integrate new objects into a scene, thanks to our explicit point-cloud-based representation. The first two figures in Fig. 7 illustrates the integration of a pre-trained toy bear in front of the mirror, and the mirror shows its reflected image.

Adding New Mirrors Likewise, we can seamlessly add a new mirror into the scene. We generate a new mirror by distributing 3D Gaussian points evenly along the plane’s surface, each sharing identical scales and rotations. As shown in the last two figures of Fig. 7, the new mirror can correctly reflect the real-world scene.

6 Conclusion and Limitation

In this paper, we propose MirrorGaussian, the first method that achieves high-quality reconstruction and real-time rendering for scenes containing mirrors. The proposed explicit point-cloud-based representation utilizes the mirror symmetry between the real-world space and the virtual mirror space. Our rasterization-based dual-rendering strategy can further leverage it to efficiently generate high-quality images in novel views, and empowers various scene editing like adding new mirrors and objects.

Even though MirrorGaussian achieves promising results in modeling mirror reflections, there are still some limitations. Our method requires mirror segmentation on input images to estimate the 3D mirror plane and mask. Additionally, our dual-rendering strategy slightly decreases the rendering speed, since we currently render and compose the real-world image and the mirror image for the whole frame. This can be further optimized by performing the dual-rendering only on the mirror region.

References

1. Andersson, P., Nilsson, J., Akenine-Möller, T., Oskarsson, M., Åström, K., Fairchild, M.D.: Flip: A difference evaluator for alternating images. *Proceedings of the ACM on Computer Graphics and Interactive Techniques* **3**(2), 15:1–15:23 (2020). <https://doi.org/10.1145/3406183> **13**
2. Barron, J.T., Mildenhall, B., Verbin, D., Srinivasan, P.P., Hedman, P.: Mip-NeRF 360: Unbounded anti-aliased neural radiance fields. In: *CVPR*. pp. 5470–5479 (2022) **11, 13**
3. Cao, J., Wang, H., Chemerys, P., Shakhrai, V., Hu, J., Fu, Y., Makoviichuk, D., Tulyakov, S., Ren, J.: Real-time neural light field on mobile devices. In: *CVPR*. pp. 8328–8337 (2023) **4**
4. Cen, J., Fang, J., Yang, C., Xie, L., Zhang, X., Shen, W., Tian, Q.: Segment any 3d gaussians. *arXiv preprint arXiv:2312.00860* (2023) **2**
5. Chan, E.R., Nagano, K., Chan, M.A., Bergman, A.W., Park, J.J., Levy, A., Aittala, M., De Mello, S., Karras, T., Wetzstein, G.: Generative novel view synthesis with 3d-aware diffusion models. In: *ICCV*. pp. 4217–4229 (2023) **3**
6. Chen, A., Xu, Z., Geiger, A., Yu, J., Su, H.: Tensorf: Tensorial radiance fields. In: *ECCV*. pp. 333–350 (2022) **4**
7. Chen, Z., Funkhouser, T., Hedman, P., Tagliasacchi, A.: Mobilenerf: Exploiting the polygon rasterization pipeline for efficient neural field rendering on mobile architectures. In: *CVPR*. pp. 16569–16578 (2023) **4**
8. Fischler, M.A., Bolles, R.C.: Random sample consensus: a paradigm for model fitting with applications to image analysis and automated cartography. *Communications of the ACM* **24**(6), 381–395 (1981) **8**
9. Franke, L., Rückert, D., Fink, L., Innmann, M., Stamminger, M.: Vet: Visual error tomography for point cloud completion and high-quality neural rendering. In: *SIGGRAPH Asia 2023 Conference Papers*. pp. 1–12 (2023) **4**
10. Franke, L., Rückert, D., Fink, L., Stamminger, M.: Trips: Trilinear point splatting for real-time radiance field rendering. *arXiv preprint arXiv:2401.06003* (2024) **4**
11. Fridovich-Keil, S., Yu, A., Tancik, M., Chen, Q., Recht, B., Kanazawa, A.: Plenoxels: Radiance fields without neural networks. In: *CVPR*. pp. 5501–5510 (2022) **4**
12. Guo, Y.C., Kang, D., Bao, L., He, Y., Zhang, S.H.: Nerfren: Neural radiance fields with reflections. In: *CVPR*. pp. 18409–18418 (2022) **4**
13. Hedman, P., Srinivasan, P.P., Mildenhall, B., Barron, J.T., Debevec, P.: Baking neural radiance fields for real-time view synthesis. In: *ICCV*. pp. 5875–5884 (2021) **4**
14. Hu, X., Wang, Y., Fan, L., Fan, J., Peng, J., Lei, Z., Li, Q., Zhang, Z.: Semantic anything in 3d gaussians. *arXiv preprint arXiv:2401.17857* (2024) **2**
15. Jiang, Y., Tu, J., Liu, Y., Gao, X., Long, X., Wang, W., Ma, Y.: Gaussianshader: 3d gaussian splatting with shading functions for reflective surfaces. *arXiv preprint arXiv:2311.17977* (2023) **2, 4**
16. Kerbl, B., Kopanas, G., Leimkühler, T., Drettakis, G.: 3d gaussian splatting for real-time radiance field rendering. *ACM Transactions on Graphics (ToG)* **42**(4), 1–14 (2023) **2, 3, 4, 5, 6, 8, 11, 12**
17. Kirillov, A., Mintun, E., Ravi, N., Mao, H., Rolland, C., Gustafson, L., Xiao, T., Whitehead, S., Berg, A.C., Lo, W.Y., et al.: Segment anything. *arXiv preprint arXiv:2304.02643* (2023) **8, 9, 12**
18. Kopanas, G., Leimkühler, T., Rainer, G., Jambon, C., Drettakis, G.: Neural point catacaustics for novel-view synthesis of reflections. *ACM Transactions on Graphics (TOG)* **41**(6), 1–15 (2022) **4, 5**

19. Kopanas, G., Philip, J., Leimkühler, T., Drettakis, G.: Point-based neural rendering with per-view optimization. In: *Computer Graphics Forum*. vol. 40, pp. 29–43. Wiley Online Library (2021) [4](#)
20. Lee, B., Lee, H., Sun, X., Ali, U., Park, E.: Deblurring 3D gaussian splatting. *arXiv preprint arXiv:2401.00834* (2024) [4](#)
21. Liang, Z., Zhang, Q., Feng, Y., Shan, Y., Jia, K.: GS-IR: 3d gaussian splatting for inverse rendering. *arXiv preprint arXiv:2311.16473* (2023) [4](#)
22. Lin, J., Li, Z., Tang, X., Liu, J., Liu, S., Liu, J., Lu, Y., Wu, X., Xu, S., Yan, Y., et al.: Vastgaussian: Vast 3D gaussians for large scene reconstruction. In: *CVPR* (2024) [2](#), [4](#)
23. Liu, Y., Wang, P., Lin, C., Long, X., Wang, J., Liu, L., Komura, T., Wang, W.: Nero: Neural geometry and brdf reconstruction of reflective objects from multiview images. *arXiv preprint arXiv:2305.17398* (2023) [2](#), [4](#)
24. Lu, T., Yu, M., Xu, L., Xiangli, Y., Wang, L., Lin, D., Dai, B.: Scaffold-gs: Structured 3D gaussians for view-adaptive rendering. In: *CVPR* (2024) [2](#), [4](#)
25. Mildenhall, B., Srinivasan, P.P., Tancik, M., Barron, J.T., Ramamoorthi, R., Ng, R.: Nerf: Representing scenes as neural radiance fields for view synthesis. In: *ECCV* (2020) [2](#), [3](#)
26. Müller, T., Evans, A., Schied, C., Keller, A.: Instant neural graphics primitives with a multiresolution hash encoding. *ACM Transactions on Graphics (TOG)* **41**(4), 1–15 (2022) [4](#), [11](#)
27. Reiser, C., Peng, S., Liao, Y., Geiger, A.: Kilonerf: Speeding up neural radiance fields with thousands of tiny mlps. In: *ICCV*. pp. 14335–14345 (2021) [4](#)
28. Reiser, C., Szeliski, R., Verbin, D., Srinivasan, P., Mildenhall, B., Geiger, A., Barron, J., Hedman, P.: Merf: Memory-efficient radiance fields for real-time view synthesis in unbounded scenes. *ACM Transactions on Graphics (TOG)* **42**(4), 1–12 (2023) [4](#)
29. Rückert, D., Franke, L., Stamminger, M.: Adop: Approximate differentiable one-pixel point rendering. *ACM Transactions on Graphics (TOG)* **41**(4), 1–14 (2022) [4](#)
30. Schonberger, J.L., Frahm, J.M.: Structure-from-motion revisited. In: *CVPR*. pp. 4104–4113 (2016) [3](#), [7](#), [12](#)
31. Shi, Y., Wu, Y., Wu, C., Liu, X., Zhao, C., Feng, H., Liu, J., Zhang, L., Zhang, J., Zhou, B., et al.: GIR: 3D gaussian inverse rendering for relightable scene factorization. *arXiv preprint arXiv:2312.05133* (2023) [4](#)
32. Shih, M.L., Su, S.Y., Kopf, J., Huang, J.B.: 3d photography using context-aware layered depth inpainting. In: *CVPR*. pp. 8028–8038 (2020) [3](#)
33. Sitzmann, V., Thies, J., Heide, F., Niefner, M., Wetzstein, G., Zollhofer, M.: Deepvoxels: Learning persistent 3d feature embeddings. In: *CVPR*. pp. 2437–2446 (2019) [3](#)
34. Srinivasan, P.P., Deng, B., Zhang, X., Tancik, M., Mildenhall, B., Barron, J.T.: NeRV: Neural reflectance and visibility fields for relighting and view synthesis. In: *CVPR*. pp. 7495–7504 (2021) [4](#)
35. Van Holland, L., Bliersbach, R., Müller, J.U., Stotko, P., Klein, R.: Tram-nerf: Tracing mirror and near-perfect specular reflections through neural radiance fields. *arXiv preprint arXiv:2310.10650* (2023) [2](#), [5](#)
36. Verbin, D., Hedman, P., Mildenhall, B., Zickler, T., Barron, J.T., Srinivasan, P.P.: Ref-nerf: Structured view-dependent appearance for neural radiance fields. In: *CVPR*. pp. 5481–5490 (2022) [4](#), [11](#), [12](#)

37. Wang, F., Rakotosaona, M.J., Niemeyer, M., Szeliski, R., Pollefeys, M., Tombari, F.: Unisdf: Unifying neural representations for high-fidelity 3d reconstruction of complex scenes with reflections. arXiv preprint arXiv:2312.13285 (2023) [4](#)
38. Wang, P., Liu, L., Liu, Y., Theobalt, C., Komura, T., Wang, W.: Neus: Learning neural implicit surfaces by volume rendering for multi-view reconstruction. NeurIPS (2021) [4](#)
39. Wiles, O., Gkioxari, G., Szeliski, R., Johnson, J.: Synsin: End-to-end view synthesis from a single image. In: CVPR. pp. 7467–7477 (2020) [3](#)
40. Yan, Z., Low, W.F., Chen, Y., Lee, G.H.: Multi-scale 3D gaussian splatting for anti-aliased rendering. arXiv preprint arXiv:2311.17089 (2023) [4](#)
41. Yang, Z., Gao, X., Sun, Y., Huang, Y., Lyu, X., Zhou, W., Jiao, S., Qi, X., Jin, X.: Spec-gaussian: Anisotropic view-dependent appearance for 3d gaussian splatting. arXiv preprint arXiv:2402.15870 (2024) [2](#)
42. Yao, Y., Zhang, J., Liu, J., Qu, Y., Fang, T., McKinnon, D., Tsin, Y., Quan, L.: NeILF: Neural incident light field for physically-based material estimation. In: ECCV. pp. 700–716 (2022) [4](#)
43. Ye, M., Danelljan, M., Yu, F., Ke, L.: Gaussian grouping: Segment and edit anything in 3d scenes. arXiv preprint arXiv:2312.00732 (2023) [2](#)
44. Yin, Z.X., Qiu, J., Cheng, M.M., Ren, B.: Multi-space neural radiance fields. In: CVPR. pp. 12407–12416 (2023) [2](#), [5](#), [11](#), [12](#)
45. Yu, Z., Chen, A., Huang, B., Sattler, T., Geiger, A.: Mip-splatting: Alias-free 3D gaussian splatting. arXiv preprint arXiv:2311.16493 (2023) [2](#), [4](#)
46. Zeng, J., Bao, C., Chen, R., Dong, Z., Zhang, G., Bao, H., Cui, Z.: Mirror-nerf: Learning neural radiance fields for mirrors with whitted-style ray tracing. arXiv preprint arXiv:2308.03280 (2023) [2](#), [5](#), [11](#), [12](#)
47. Zwicker, M., Pfister, H., Van Baar, J., Gross, M.: Ewa splatting. IEEE Transactions on Visualization and Computer Graphics **8**(3), 223–238 (2002) [5](#)